



# Assessment of a white matter reference region for $^{11}\text{C}$ -UCB-J PET quantification

Samantha Rossano<sup>1,2</sup>, Takuya Toyonaga<sup>1</sup>, Sjoerd J Finnema<sup>1</sup> , Mika Naganawa<sup>1</sup> , Yihuan Lu<sup>1</sup>, Nabeel Nabulsi<sup>1</sup>, Jim Ropchan<sup>1</sup>, Steven De Bruyn<sup>3</sup>, Christian Otoul<sup>3</sup>, Armel Stockis<sup>3</sup>, Jean-Marie Nicolas<sup>3</sup>, Paul Martin<sup>3</sup>, Joel Mercier<sup>3</sup>, Yiyun Huang<sup>1</sup>, R Paul Maguire<sup>3</sup> and Richard E Carson<sup>1,2</sup>

## Abstract

$^{11}\text{C}$ -UCB-J is a positron emission tomography (PET) radioligand that has been used in humans for synaptic vesicle glycoprotein 2A (SV2A) imaging and as a potential synaptic density marker. The centrum semiovale (CS) is a proposed reference region for noninvasive quantification of  $^{11}\text{C}$ -UCB-J, due to negligible concentrations of SV2A in this region in baboon brain assessed by in vitro methods. However, in displacement scans with SV2A-specific drug levetiracetam in humans, a decrease in  $^{11}\text{C}$ -UCB-J concentration was observed in the CS, consistent with some degree of specific binding. The current study aims to validate the CS as a reference region by (1) optimizing CS region of interest (ROI) to minimize spill-in from gray matter with high radioactivity concentrations; (2) investigating convergence of CS ROI values using ordered subset expectation maximization (OS-EM) reconstruction, and (3) comparing baseline CS volume of distribution ( $V_T$ ) to nondisplaceable uptake in gray matter,  $V_{ND}$ . Improving ROI definition and increasing OS-EM iterations during reconstruction decreased the difference between CS  $V_T$  and  $V_{ND}$ . However, even with these corrections, CS  $V_T$  overestimated  $V_{ND}$  by  $\sim 35$ – $40\%$ . These measures showed significant correlation, suggesting that, though biased, the CS may be a useful estimate of nondisplaceable uptake, allowing for noninvasive quantification for SV2A PET.

## Keywords

Ordered subset expectation maximization reconstruction, positron emission tomography, reference region, synaptic vesicle glycoprotein 2A, synaptic density

Received 4 April 2019; Accepted 14 August 2019

## Introduction

Synaptic vesicle proteins, including the synaptic vesicle glycoprotein 2A (SV2A), are of interest for their roles in neurological and neurodegenerative disorders, including epilepsy<sup>1</sup> and Alzheimer's disease (AD).<sup>2</sup> As such, SV2A has become a target of interest for development of positron emission tomography (PET) radioligands, in order to evaluate SV2A distribution in vivo. The current work employed  $^{11}\text{C}$ -UCB-J; other SV2A-specific radioligands include  $^{11}\text{C}$ -UCB-A, which has good affinity for SV2A but exhibits slow binding kinetics in pig<sup>3</sup> and monkey;<sup>4</sup>  $^{18}\text{F}$ -UCB-H, a molecule which has a relatively low affinity for SV2A (in vitro  $K_i = \sim 50$  nM)<sup>5</sup> and a low gray-to-white matter contrast in the nonhuman primate and human brain; and  $^{18}\text{F}$ -SDM-8,<sup>6</sup> the most-recently developed SV2A

PET radioligand which has a high affinity (in vitro  $K_i = 0.58$  nM), high gray-to-white matter contrast and has been used in nonhuman primates.

$^{11}\text{C}$ -UCB-J has comparable SV2A affinity to  $^{18}\text{F}$ -SDM-8 and has been used for imaging in both non-human primates<sup>4</sup> and humans to investigate changes in

<sup>1</sup>Department of Radiology and Biomedical Imaging, Yale PET Center, Yale School of Medicine, New Haven, CT, USA

<sup>2</sup>Department of Biomedical Engineering, Yale University, New Haven, CT, USA

<sup>3</sup>UCB Pharma, Brussels, Belgium

## Corresponding author:

Samantha Rossano, Department of Radiology and Biomedical Imaging, Yale PET Center, Yale School of Medicine, P.O. Box 208048, New Haven, CT 06513, USA.

Email: samantha.rossano@yale.edu

synaptic density in epilepsy patients<sup>7</sup> and patients with mild cognitive impairment and AD.<sup>8</sup> Initial studies included dynamic PET acquisitions analyzed with compartment models using the metabolite-corrected arterial input functions.<sup>9</sup> However, in order for PET radioligands to be conveniently applied in the clinic setting, it would be preferred to apply noninvasive methods to attain meaningful quantitative measurements of the target of interest, such as reference region methods. Reference region methods allow for the quantification of the binding potential with respect to the nondisplaceable compartment,  $BP_{ND}$ . If an ideal reference region exists for a radioligand, then the total uptake in the reference region ( $V_T^{Ref}$ ) should be equivalent to the nondisplaceable (i.e. free + non-specifically bound radioligand) uptake in the remaining regions of interest (ROIs),  $V_{ND}$ . In other words, there should be no specific or displaceable uptake in the reference region.

For noninvasive quantification with  $^{11}C$ -UCB-J, the white matter region of the centrum semiovale (CS) was proposed as a reference region, due to its low PET uptake compared to cortical and subcortical gray matter in nonhuman primates and humans and its low concentration of SV2A compared to gray matter regions of the baboon brain shown by *in vitro* methods.<sup>7</sup> However, as reported in the first-in-human study, during displacement scans using SV2A specific drug levetiracetam (LEV),  $^{11}C$ -UCB-J concentration decreased by about 10–15% in the CS, indicating the presence of some degree of specific binding in that region.<sup>7</sup> In this work, we further carefully characterize  $^{11}C$ -UCB-J binding in the CS, initially by optimizing the CS ROI definition to minimize the inclusion of gray matter and any partial volume effects that would cause spill over and thus an overestimation of baseline  $V_T$ . Additionally, convergence using the ordered subset expectation maximization (OS-EM) reconstruction algorithm was investigated by increasing the iterations used to reconstruct the PET image; this would minimize any positive bias that may be observed in the low-intensity white matter, surrounded by the high-intensity gray matter. Lastly, baseline and blocking  $^{11}C$ -UCB-J scans were used to estimate the  $V_{ND}$  of the gray matter, and the validity of using CS  $V_T$  to estimate  $V_{ND}$  in calculating  $BP_{ND}$  was evaluated.

## Materials and methods

### Participants and PET scanning conditions

Firstly, a group of 52 healthy subjects (M/F = 34/18; age:  $48 \pm 19$ ) received  $^{11}C$ -UCB-J scans and magnetic resonance imaging (MRI) for anatomic definition. Image data from these subjects were used to optimize the CS ROI definition (see below). For evaluation of

$^{11}C$ -UCB-J binding under baseline and blocking conditions, participants and study design were completed as previously described.<sup>10</sup> A total of 13 healthy subjects (M/F = 7/6; age:  $31 \pm 8$ ) received 120-min baseline and blocking  $^{11}C$ -UCB-J scans with LEV and/or bivaracetam (BRV). Seven of 13 subjects received baseline and blocking  $^{11}C$ -UCB-J scans with both LEV (250, 600, or 1500 mg) and BRV (50, 100, or 200 mg). Two of 13 subjects received blocking  $^{11}C$ -UCB-J scans with only BRV, and 4 of 13 received blocking  $^{11}C$ -UCB-J scans with only LEV. In 9 of 13 baseline cases, the blocking drug was administered as a displacement 60 min after  $^{11}C$ -UCB-J administration, so for this reason, the first 60 min of the PET data were used for analysis of baseline and blocking scans. Four of the 13 subjects received repeated dosing of BRV (50 or 100 mg), orally twice daily. A baseline  $^{11}C$ -UCB-J scan was acquired prior to the first BRV dose, followed by an acute post-dose  $^{11}C$ -UCB-J scan. Three days after repeated dosing, a post-dose  $^{11}C$ -UCB-J scan was acquired 1 to 2 h after the morning BRV dose was taken (“peak”). Later the same day, a post-dose  $^{11}C$ -UCB-J scan was acquired approximately 8 h after the last BRV dose (“trough”). In total, 28 blocking scans were performed. This study was performed under a protocol approved by the Yale University Human Investigation Committee and the Yale New Haven Hospital Radiation Safety Committee, in accordance with the United States federal policy for the protection of human research subjects contained in Title 45 Part 46 of the Code of Federal Regulations (45 CFR 46). Written informed consent was obtained from all participants after complete explanation of study procedures.

### PET data acquisition

$^{11}C$ -UCB-J was prepared using previously described methods.<sup>4</sup> Dynamic PET measurements were acquired in listmode format on the Siemens high-resolution research tomograph (HRRT) using a bolus plus constant infusion<sup>11</sup> paradigm of  $^{11}C$ -UCB-J ( $K_{bol} = 150$ ), with the bolus injection over 1 min. Prior to PET acquisition, a 6-min transmission scan was performed with a  $^{137}Cs$  point source for attenuation correction. MRI T1-weighted anatomical images were acquired using a Siemens Trio 3T MRI scanner. During PET scanning, arterial blood samples were collected every 10 s for the first 90 s, followed by 1.75, 2, 2.25, 2.5, 2.75, 3, 4, 5, 6, 8, 10, 15, 20, 25, 30, 45, 60, 75, 90, 105, and 120 min after  $^{11}C$ -UCB-J injection. Whole blood and plasma samples were analyzed for radioactivity concentration. Plasma samples at 3, 8, 15, 30, 60, and 90 min were also used for metabolite analyses to estimate the unmetabolized  $^{11}C$ -UCB-J fraction.

### Image reconstruction and registration

Dynamic PET data were reconstructed using the motion-compensation OS-EM listmode algorithm for resolution-recovery reconstruction (MOLAR<sup>12</sup>) into 21 frames: (6 × 30 s, 3 × 1 min, 2 × 2 min, and 10 × 5 min) with corrections for attenuation, randoms, scatter, normalization, and dead time. Head motion detected by a Polaris Vira optical tracking system was used for event-by-event motion correction during image reconstruction.<sup>13</sup> Dynamic images were reconstructed with 2 iterations of 30 subsets (2i, standard), as well as 3 and 4 iterations of 30 subsets (3i and 4i) to assess convergence of the white matter region of the CS. Dimensions and voxel size of PET images were: 256 × 256 × 207 and 1.21875 × 1.21875 × 1.231 mm, respectively.

To account for any residual motion, reconstructed dynamic images were motion corrected by registering each frame to an early summed PET image using linear registration (6-parameter mutual information algorithm FLIRT of FSL). An early sum of the motion corrected PET image was then coregistered to the subject's T1-weighted MRI (6-parameter rigid registration), and the subject MRI was coregistered to the automated anatomical labeling AAL template in the Montreal Neurological Institute (MNI) space using a non-linear transformation (BioImage Suite, www.bioimagesuite.org).<sup>14</sup>

### Optimal white matter CS ROI definition

In our previous work,<sup>7</sup> the white matter region of the CS was originally defined manually on the AAL template and shrunk by two voxels in each direction, for a total ROI volume of 5.86 mL in template space, to minimize partial volume effect (CS<sub>orig</sub>). However, in an attempt to further minimize potential spill-in from gray matter regions with high radioactivity concentrations into the low-radioactivity containing white matter region, caused by the partial volume effect, additional methods were investigated to define this ROI. Each subject's MRI was segmented using SPM12 and the resulting WM probability map was smoothed with a 10-mm FWHM Gaussian filter, to ensure inclusion of the core of the CS. This smoothed WM map was masked by the AAL template of CS registered to each subject's space. Within this masked map, CS ROI sizes of 2, 4, and 6 mL volumes (CS<sub>2</sub>, CS<sub>4</sub>, CS<sub>6</sub>) were created from the voxels with the highest WM probability in the smoothed WM map. The 2-mL CS ROI mask images from all subjects were transformed to MNI space and averaged. The final ROI was created by selecting the voxels that had the highest average values to create a ROI volume of 2 mL in template space; this template was denoted CS<sub>AAL</sub>.

### Image quantification and analysis

Regional time activity curves were analyzed using the one-tissue compartment model (1TCM),<sup>9,15</sup> using the arterial input function and the first 60 min of time activity data. The total volume of distribution  $V_T$ , the sum of the specific volume of distribution  $V_S$ , and the non-displaceable volume of distribution  $V_{ND}$ , was estimated as  $K_1/k_2$  for each ROI and scan condition for the following 23 gray matter (GM) ROIs: amygdala, anterior cingulum, anterior insula, caudate, cerebellum, dorsolateral prefrontal cortex, frontal cortex, fusiform, hippocampus, insula, occipital cortex, orbitofrontal cortex, pallidum, parahippocampal region, parietal cortex, posterior cingulum, posterior insula, putamen, substantia nigra, temporal cortex, thalamus, ventral striatum, ventromedial prefrontal cortex, and the multiple CS ROIs. Blood volume fraction was not included in the kinetic evaluation, as it has been shown to have negligible effects on both  $K_1$  and  $V_T$  as shown in Supplemental Figure 1 of Finnema et al.<sup>9</sup>

For each blocking study, the receptor occupancy ( $r$ ) and the  $V_{ND}$  were determined using the Lassen Occupancy plot.<sup>16</sup> In summary, the difference in  $V_T$  between a blocking scan and the corresponding baseline scan were plotted against the baseline  $V_T$  values for each GM ROI. Graphically, the occupancy is defined as the slope of the best-fit line, while the x-intercept is equal to the  $V_{ND}$ . Mathematically, if  $V_T^{\text{Base}} = V_{ND} + V_S$  and  $V_T^{\text{Drug}} = V_{ND} + (1 - r) \times V_S$ , then the difference between these expressions is  $V_T^{\text{Base}} - V_T^{\text{Drug}} = r \times V_S$ . Substituting  $V_T^{\text{Base}} - V_{ND}$  for  $V_S$

$$V_T^{\text{Base}} - V_T^{\text{Drug}} = r \times (V_T^{\text{Base}} - V_{ND}) \quad (1)$$

This analysis was performed for each pair of baseline and blocking scans, using reconstructed images with 2, 3, and 4 OS-EM iterations (all with 30 subsets).

To examine possible heterogeneities in regional  $V_{ND}$  and  $V_S$ , parametric images of these parameters were created using parametric  $V_T$  images of baseline and blocking scans, which were generated using voxel-wise fitting of the 1TCM as described previously,<sup>9</sup> and the plasma concentration of BRV during blocking <sup>11</sup>C-UCB-J scans. Parametric  $V_T$  images were produced by voxel-wise fitting of 1–60 min of dynamic PET images to the 1TCM and were registered to MNI template space. Images from nine pairs of baseline and acute-post-dose scans with BRV, reconstructed with 2 OS-EM iterations, were used to estimate  $V_{ND}$  and  $V_S$  at each voxel  $i$  using  $V_T$  data from each subject  $j$ , with equation (2)

$$V_{T,i,j} = V_{ND,i} + (1 - r_j) \times V_{S,i} \quad (2)$$

where  $r_j=0$  for baseline scans, and  $r_j$  was calculated using the average drug concentration in blood during the post-dose scan,  $c$ , and the  $IC_{50}$  for BRV, which was fixed at  $0.46 \mu\text{g/mL}$ ,<sup>10</sup> as shown in equation (3)

$$r_j = \frac{c_j}{c_j + IC_{50}} \quad (3)$$

From this, parametric  $V_{ND}$  and  $V_S$  images were created with voxel-by-voxel linear regression of the 18  $V_T$  values (9 subjects  $\times$  2 scans each) to estimate  $V_{ND}$  and  $V_S$  for each voxel.

The PET outcome measure of binding potential,  $BP$ , is indicative of in vitro measurements  $B_{\text{max}}/K_D$ , or the product of target density and the affinity of the radioligand for the target.  $BP_{ND}$  is the binding potential with respect to the nondisplaceable compartment, and can be calculated by using the following

$$BP_{ND} = \frac{V_T - V_{ND}}{V_{ND}} \quad (4)$$

If a reference region exists such that the total uptake in the reference region represents the free and nondisplaceable uptake in the gray matter, then equation (4) becomes

$$\widehat{BP}_{ND} = \frac{V_T - V_T^{\text{Ref}}}{V_T^{\text{Ref}}} \quad (5)$$

To determine the efficacy of substituting the  $V_T$  of the CS for  $V_{ND}$ ,  $BP_{ND}$  was calculated from baseline scans for the 23 ROIs for a subset of subjects ( $N=7$ ) using the extrapolated  $V_{ND}$  from the Lassen plots for each subject ( $BP_{ND}^{\text{True}}$ ), as well as the  $V_T$  in the CS at 2 and 4 iterations (2i and 4i) of 30 subsets ( $\widehat{BP}_{ND}^{2i}$  and  $\widehat{BP}_{ND}^{4i}$ ). Calculated  $BP_{ND}$  values were plotted against true  $BP_{ND}$  to assess discrepancies from ground truth by deviation from the unity line.

For evaluating changes in outcome measures due to increasing OS-EM iterations, one-way ANOVA (or its non-parametric equivalent, Friedman test) tests were used with post-hoc testing for multiple comparisons when appropriate. Differences between two values (i.e., baseline CS  $V_T$  vs.  $V_{ND}$ ) were analyzed using the Student's  $t$  test or non-parametric equivalent, Mann Whitney test. For subjects who received chronic dosing of BRV with a single baseline scan and multiple post-dose scans, the baseline CS  $V_T$  values were used only once in estimation of group statistics, and the blocking CS  $V_T$  values and  $V_{ND}$  estimates from these studies were averaged before evaluating group statistics.

## Results

### Optimal white matter CS ROI

Of the 52 subjects used to define CS ROIs, 47 subjects had an arterial input function for  $V_T$  estimation with ITCM. The baseline  $V_T$  values estimated using a 1 T fit of the dynamic PET data in the five CS ROIs investigated are shown in Figure 1(a). The template ROI derived from the average of all subjects' WM probability maps at 2 mL (CS\_AAL) had the lowest  $V_T$  values and comparable variability across subjects ( $\sim 13.3\%$  coefficient of variation) compared to the ROIs defined on individual WM probability maps (CS\_2, CS\_4, CS\_6, with 12.4%, 12.1%, and 12.1% coefficient of variation, respectively) and compared to the original CS region (CS\_orig, with 13.6% coefficient of variation). Using CS\_orig, the mean  $\pm$  SD  $V_T$  was  $4.93 \pm 0.67$ , which decreased by 12.8% to  $4.30 \pm 0.57$  when using the CS\_AAL region. These lower  $V_T$  values suggest that the new ROI potentially includes less spill-in from surrounding high-activity gray matter regions. Reducing such spill-in will also contribute to a decrease in the difference of CS  $V_T$  between baseline and blocking scans. Further, the CS\_AAL region better represents the white matter region across subjects by avoiding the gray matter-white matter boundary better than the CS\_orig ROI, as shown on a representative subject's MRI and PET image in Figure 1(b) and (c). Thus, the CS\_AAL region was used for quantification and analysis.

### CS $V_T$ at higher OS-EM iterations

Representative baseline and blocking  $V_T$  images are shown in Figure 2(a) and (b). Occupancy measures derived from the Lassen plot, shown for this representative subject in Figure 2(c), range from 50.0% to 87.3% and do not significantly change with higher OS-EM iterations. Increasing the number of OS-EM iterations had negligible effects on baseline and blocking  $V_T$  values in gray matter ROIs, with percent increases of 1.7 ( $\pm 0.8$ )% and 1.3 ( $\pm 0.3$ )% from 2 to 4 iterations. This was not the case in white matter, where increasing the number of OS-EM iterations decreased the CS baseline  $V_T$  by  $8.5 \pm 5.8\%$ , from an average ( $\pm$ SD) of  $4.58 \pm 0.64 \text{ mL/cm}^3$  at 2i to  $4.21 \pm 0.74 \text{ mL/cm}^3$  at 4i ( $N=13$ ,  $p < 0.0001$ , Friedman/ANOVA, Figure 3(a)). Additional OS-EM iterations did not have a significant effect on CS  $V_T$  during blocking scans, changing from  $3.60 \pm 0.54$  at 2i to  $3.64 \pm 0.65 \text{ mL/cm}^3$  at 4i ( $N=28$ ,  $p=0.1292$ , Friedman/ANOVA, Figure 3(b)).

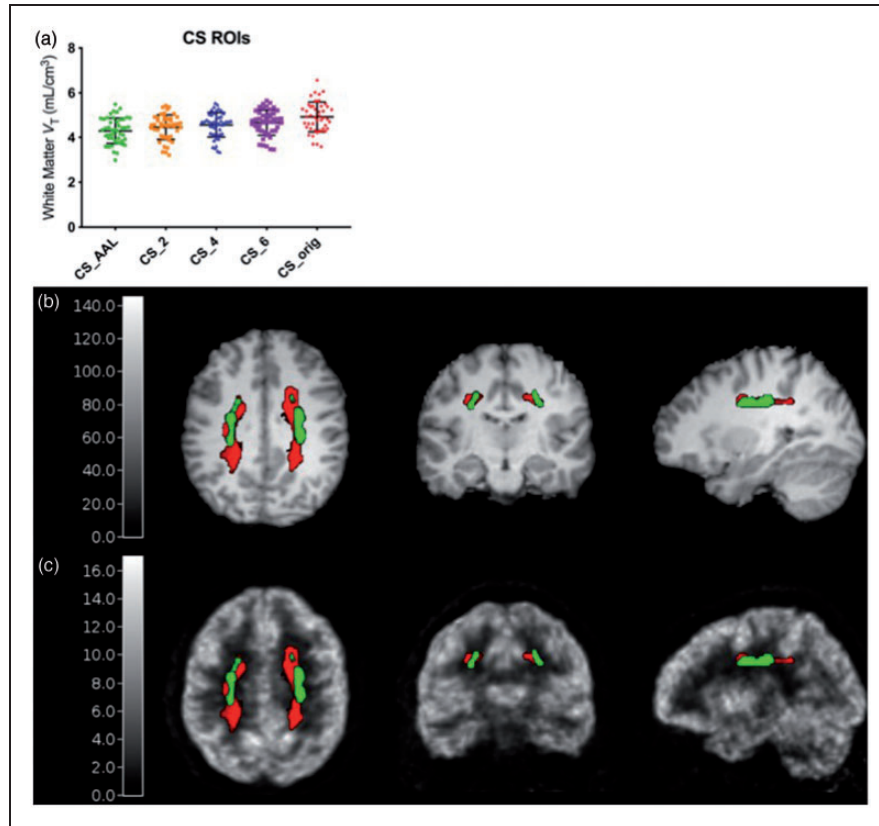


**Figure 1.** Optimization of the centrum semiovale reference region. (a)  $V_T$  values from 47 subjects using centrum semiovale (CS) regions averaged across multiple subjects in AAL space (CS\_AAL), regions defined from each subjects' individual probability maps with 2-, 4-, and 6-mL volumes (CS\_2, CS\_4, and CS\_6), and the original CS region that was manually drawn on the MNI template, eroded by two voxels in each direction (CS\_orig). Error bars indicate 1 standard deviation from the mean. CS\_orig (red diamonds) and CS\_AAL (green circles) ROIs overlaid on a representative subject's MRI (b) and  $^{11}\text{C}$ -UCB-J scan (c, SUV, units: g/mL).

### Blockade of $^{11}\text{C}$ -UCB-J uptake in CS

Significant decreases in CS  $V_T$  were observed between baseline and blocking conditions at 2i (Figure 3(c)). On average, the percent difference between a subject's corresponding baseline and blocking scan was  $22.0 \pm 10.8\%$  at 2i. This difference decreased to  $16.4 \pm 12.0\%$  at 4i, though the difference in  $V_T$  values between baseline and blocking remained statistically significant under this condition (Figure 3(d)). These differences were not associated with SV2A occupancy estimates at 2i ( $R^2 < 0.01$ ,  $p = 0.76$ , data not shown) and at 4i ( $R^2 = 0.01$ ,  $p = 0.56$ , data not shown).

### CS $V_T$ overestimates gray matter nondisplaceable uptake

A total of 28 blocking studies were paired with their corresponding baseline scans to estimate occupancy

and  $V_{ND}$  by the Lassen Occupancy plot<sup>10</sup> using 23 GM ROIs. Three of the 28 estimated  $V_{ND}$  values were removed as outliers, due to their high percentage standard error ( $>25\%$ ). These cases corresponded to lower occupancy studies ( $r < 63\%$ ).

The estimated  $V_{ND}$  increased slightly with increasing iterations, from  $2.82 (\pm 0.35)$  mL/cm<sup>3</sup> at 2i to  $2.97 (\pm 0.37)$  mL/cm<sup>3</sup> at 4i (ANOVA,  $p = 0.02$ , Figure 4(a)). Baseline CS  $V_T$  exceeded this estimate of nondisplaceable uptake by 62% at 2i and 42% at 4i. Post-dose CS  $V_T$  also exceeded  $V_{ND}$  estimates by 27% at 2i and 23% at 4i. The differences between baseline CS  $V_T$  and gray matter  $V_{ND}$  were statistically significant at both 2 and 4 iterations ( $p < 0.0001$ , Mann Whitney  $U$  test, Figure 4(b) and (c)).

### Parametric images of $V_{ND}$

A subject's MRI in template space and the average ( $N = 9$ ) baseline  $V_T$  images are shown in Figure 5(a)

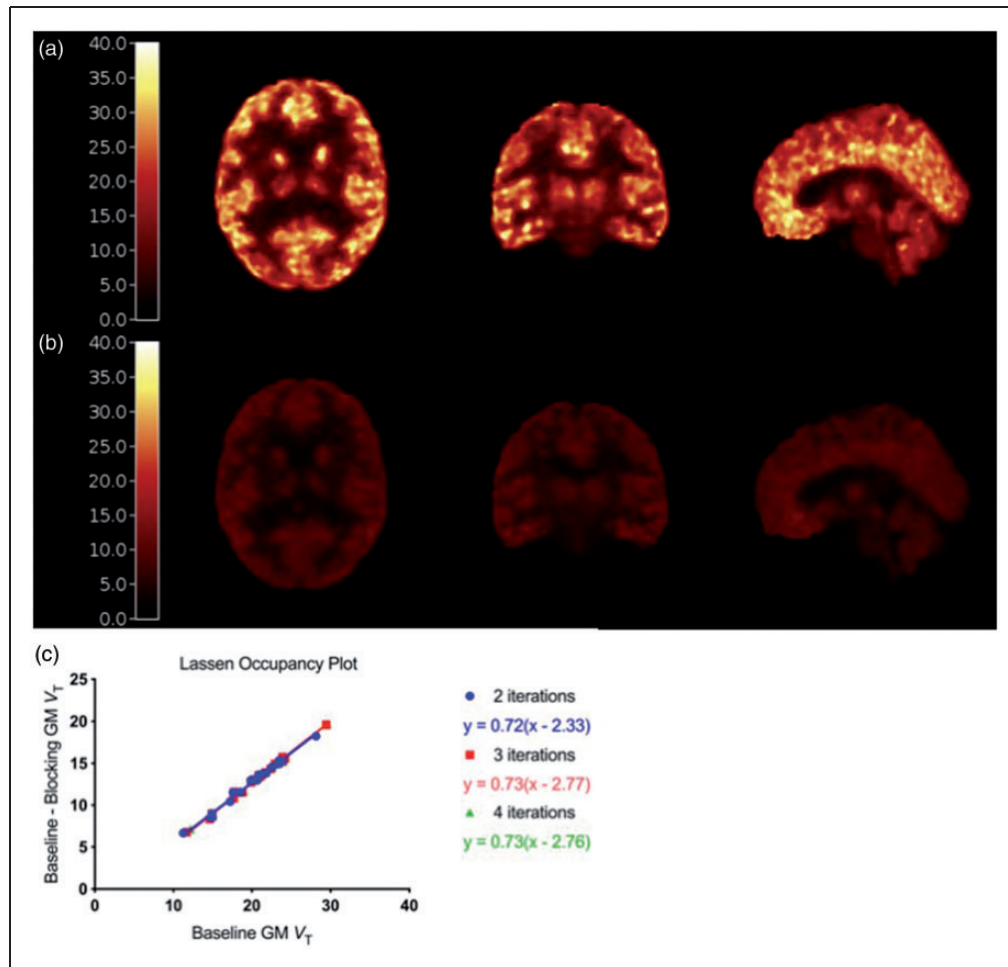


**Figure 2.** (a) Baseline and (b) blocking parametric  $V_T$  images from a representative  $^{11}\text{C}$ -UCB-J scan. (c) Lassen Occupancy plots using  $V_T$  values from two (blue circles), three (red squares), and four (green triangles) iterations of the representative subject.

and (b), respectively. Voxel-wise estimation of  $V_S$  resulted in heterogeneous values in the brain (Figure 5(c)). Template ROIs were applied to this image and the average  $V_S$  values ( $\pm\text{SD}$  across ROIs) were  $18.2 \pm 1.9 \text{ mL/cm}^3$  in the gray matter regions (frontal cortex, temporal cortex, caudate, putamen, and hippocampus) and  $1.46 \text{ mL/cm}^3$  in the CS\_AAL ROI ( $\sim 8\%$  of the GM value).

Voxel-wise parametric maps of  $V_{\text{ND}}$  also demonstrated heterogeneous values in the brain (Figure 5(d)). The average  $V_{\text{ND}}$  in the gray matter regions was  $2.81 \pm 0.24 \text{ mL/cm}^3$ , which was less than the CS, where  $V_{\text{ND}}$  was  $3.38 \text{ mL/cm}^3$ . Thus, CS nondisplaceable uptake of  $^{11}\text{C}$ -UCB-J was  $\sim 20\%$  higher than GM values. This CS  $V_{\text{ND}}$  was 6% less than the average blocking  $V_T$  in the CS, which was  $3.58 \pm 0.25$  for this subset of studies, noting that the occupancy was  $<100\%$ . It appears that  $V_{\text{ND}}$  varies slightly in other brain regions, which requires further investigation.

#### Using CS as a reference region underestimates $BP_{\text{ND}}$

Although there are differences in the values of  $V_T$  in the CS and  $V_{\text{ND}}$  of the GM, and differences are observed between gray and white matter in the parametric images of  $V_{\text{ND}}$ , the CS region has potential utility as a reference region. Across subjects, the estimates of CS  $V_T$  and GM  $V_{\text{ND}}$  were significantly correlated at both 2 ( $R^2 = 0.39$ ,  $p = 0.04$ , Figure 6(a)) and 4 iterations ( $R^2 = 0.41$ ,  $p = 0.03$ , Figure 6(b)). Interestingly, this relationship has an intercept very close to zero at 4 iterations. These correlations support the use of CS  $V_T$  as an estimate, although biased, of nondisplaceable uptake.

Using the CS  $V_T$  as a surrogate for  $V_{\text{ND}}$  results in an underestimation of  $BP_{\text{ND}}$  (Figure 6(c)). The degree of underestimation is a function of regional  $V_T$ , but ranges from 43% to 55% when using the baseline CS  $V_T$  at 2i. This range decreases slightly to between 35% and 41% when using the baseline CS  $V_T$  at 4i.

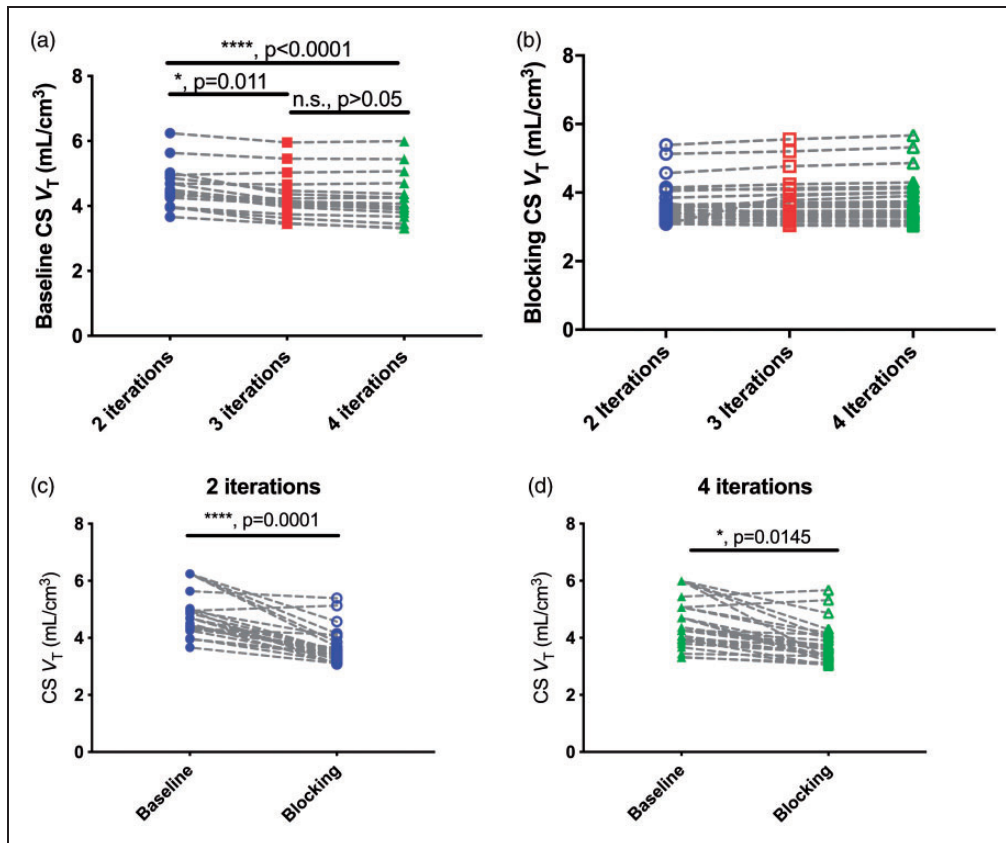


**Figure 3.** (a) Individual ( $N=13$ ) centrum semiovale (CS) volume of distribution,  $V_T$  at baseline from images reconstructed with 2, 3, and 4 OS-EM iterations of 30 subsets. Results from post-hoc testing with Dunn's multiple comparison test are shown as  $p$  values. (b) Individual ( $N=28$ )  $V_T$  under blocking conditions from images reconstructed with 2, 3, and 4 OS-EM iterations. (c) Average baseline (filled circles) and blocking (open circles)  $V_T$  at 2 OS-EM iterations. (d) Average baseline (filled circles) and blocking (open circles)  $V_T$  at 4 OS-EM iterations. For (c) and (d), results from Mann-Whitney  $U$  test are shown as  $p$  values.

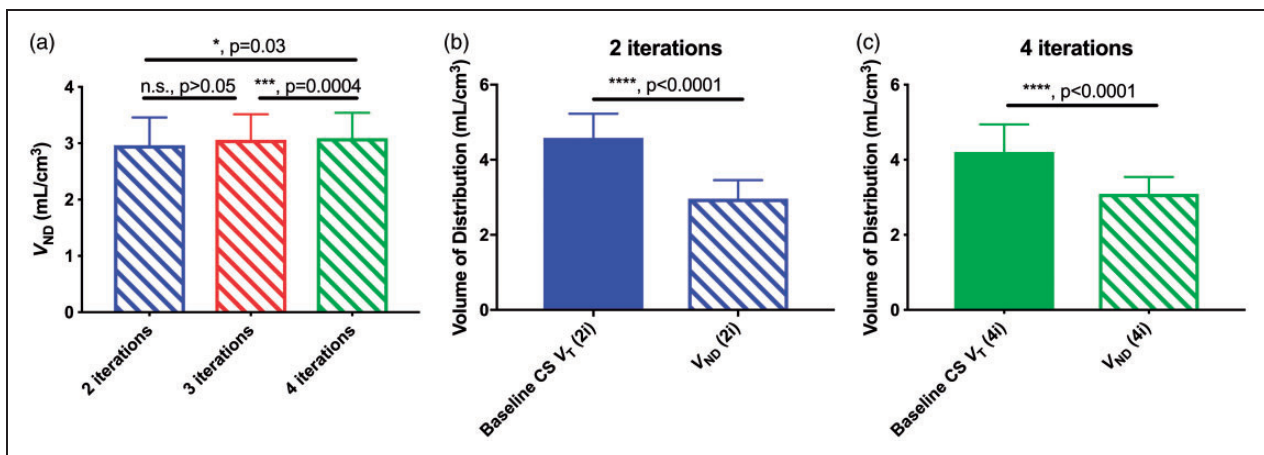


**Figure 4.** (a) Average ( $N=25$ ) nondisplaceable volume of distribution,  $V_{ND}$ , estimates at 2, 3, and 4 OS-EM iterations. Results from post-hoc testing using Tukey's multiple comparisons test resulted in significant differences between 2i and 4i, and between 3i and 4i. (b) Baseline  $V_T$  and  $V_{ND}$  estimates at 2i30s ( $p < 0.0001$ , Mann-Whitney  $U$  test). (c) Baseline  $V_T$  and  $V_{ND}$  estimates at 4i30s ( $p < 0.0001$ , Mann-Whitney  $U$  test). Error bars represent standard deviation from the mean.

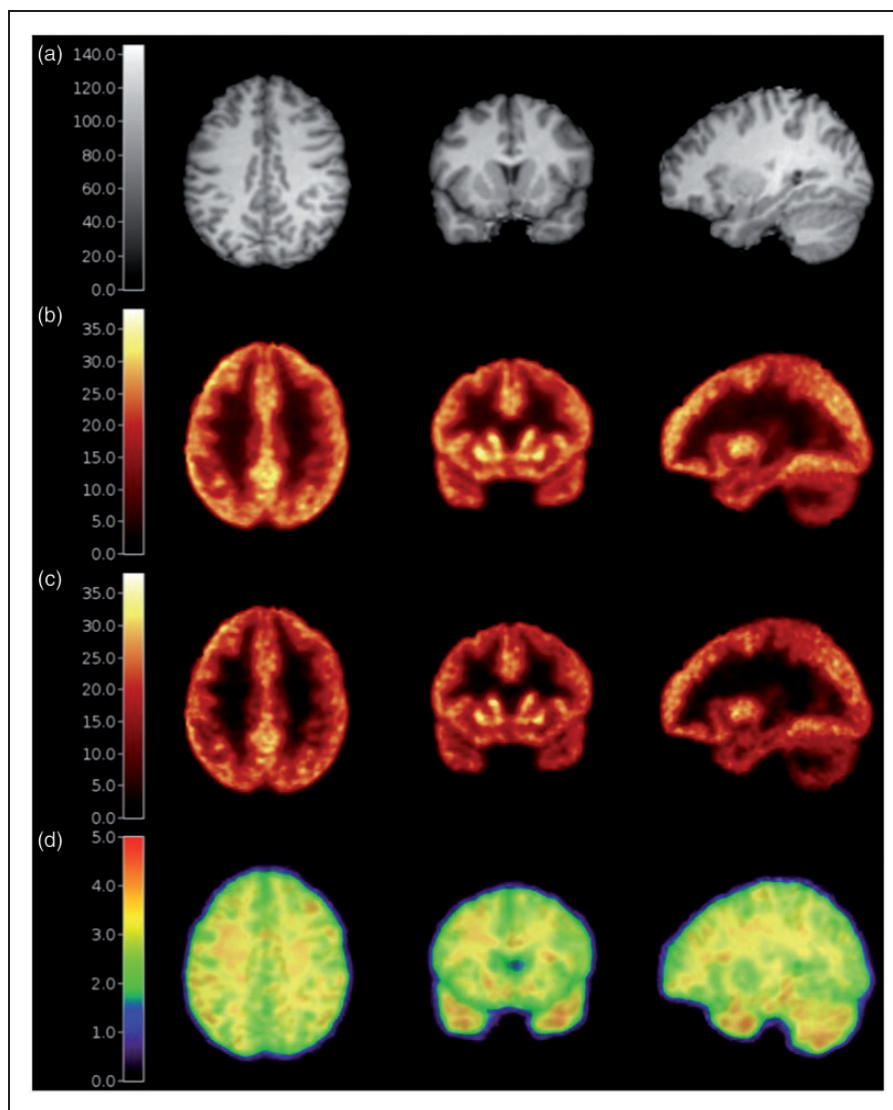


**Figure 5.** (a) Representative subject's anatomical MRI, (b) average ( $n=9$ ) baseline parametric  $V_T$ , (c) parametric images of  $V_S$ , and (d)  $V_{ND}$  overlaid on the MRI.

## Discussion

$^{11}\text{C}$ -UCB-J is a PET ligand that binds selectively to SV2A and has been proposed as a quantitative imaging biomarker for synaptic density. The CS has been proposed as a reference region in  $^{11}\text{C}$ -UCB-J PET quantification due to its minimal concentration of SV2A compared to gray matter regions in the baboon brain; however, displaceable activity was observed in the CS during LEV displacement studies in humans.<sup>7</sup> In this study, we examined the utility of CS as a reference region. First, the size and location of the CS ROI were optimized and the number of OS-EM iterations used to reconstruct the PET images was increased. These changes decreased, but did not eliminate the displaceable  $^{11}\text{C}$ -UCB-J uptake in the CS, with the  $V_T$  in the CS overestimating GM  $V_{ND}$  by 36%. Thus, if the

CS is used as a reference region,  $BP_{ND}$  is negatively biased by 40–55% (2 iterations) or 35–40% (4 iterations). However, the CS region may still be the best general-purpose reference region available for  $^{11}\text{C}$ -UCB-J PET image quantification, given the correlations of CS  $V_T$  with gray matter  $V_{ND}$  values.

This work also presents a method to create parametric maps of  $V_{ND}$  and  $V_S$  using  $V_T$  maps from baseline and blocking scans, plasma drug concentrations, assuming a constant  $IC_{50}$  value for BRV. A potential limitation is the use of a fixed  $IC_{50}$  value across all brain regions. However, when extending the two-parameter model (equation (2)) to fit regional  $V_T$  data from these nine pairs of scans to a three-parameter model to also estimate regional  $IC_{50}$  in addition to  $V_{ND}$  and  $V_S$ , the GM regions of the frontal cortex, temporal cortex, hippocampus, and putamen provided highly consistent  $IC_{50}$  estimates:



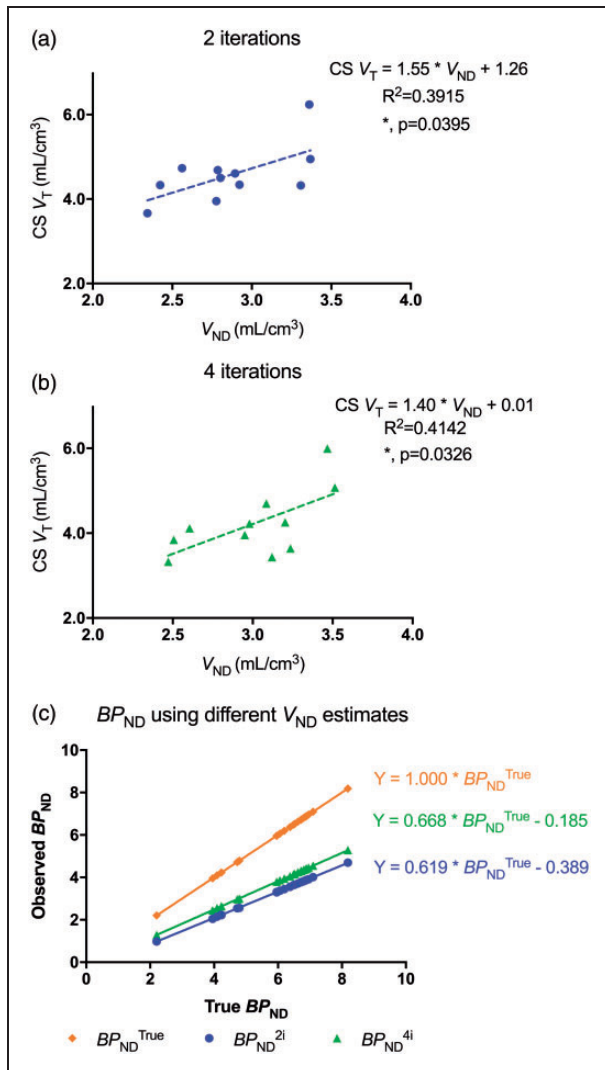


**Figure 6.** (a) Linear regression analyses of baseline CS  $V_T$  and gray matter  $V_{ND}$  at 2i ( $R^2 = 0.3915$ ,  $p = 0.04$ ). (b) Linear regression analyses of baseline CS  $V_T$  and gray matter  $V_{ND}$  at 4i ( $R^2 = 0.4142$ ,  $p = 0.03$ ). Each dot in (a) and (b) represents data from one subject. (c) Average  $BP_{ND}$  values from a subset of seven subjects in 23 ROIs, calculated using  $V_{ND}$  from blocking studies (gold diamonds,  $BP_{ND}^{True}$ ), baseline CS  $V_T$  at 2i (blue circles,  $BP_{ND}^{2i}$ ) and 4i (green triangles,  $BP_{ND}^{4i}$ ) as estimates of nondisplaceable  $^{11}\text{C}$ -UCB-J uptake.

average ( $\pm$ SD) of  $0.38 (\pm 0.03)$   $\mu\text{g}/\text{mL}$ . Reliable estimates of  $IC_{50}$  in WM could not be obtained.

We hypothesize that the difference between white matter uptake and the true nondisplaceable  $^{11}\text{C}$ -UCB-J uptake in gray matter is attributable to three causes: (1) lack of convergence with OS-EM algorithm in white matter, (2) a small amount of true specific binding in the white matter, and (3) lipophilicity differences between gray and white matter.

OS-EM is an iterative reconstruction algorithm which is used routinely in PET imaging due to its lower noise

compared to filtered backprojection algorithms.<sup>12,17</sup> It has been reported in reconstructions of objects in which a low-radioactivity region is surrounded by a high-radioactivity region with high contrast, OS-EM tends to overestimate the activity within the low activity region. This bias is corrected, as the activity in the OS-EM image converges with increased iterations.<sup>18</sup> A caveat is that image noise increases with higher OS-EM iterations, so extra iterations should only be used for regions that might have not converged with standard methods. In the case of baseline  $^{11}\text{C}$ -UCB-J scans, the CS has relatively low radioligand uptake compared to the high-radioactivity GM regions that surround it (Figure 2(a)). When we increase the number of iterations used to reconstruct these images, the positive CS bias with typical reconstruction parameters (2 iterations of 30 OS-EM subsets) was minimized. Increasing the number of iterations decreased the difference between baseline and blocking CS  $V_T$ , as well as between baseline CS  $V_T$  and GM  $V_{ND}$ ; however, there is still a significant difference between these values after correcting for the overestimation bias caused by OS-EM convergence.

Although negligible concentrations of SV2A were reported using in vitro analysis in the CS in the baboon brain,<sup>7</sup> we reported displaceable in vivo  $^{11}\text{C}$ -UCB-J uptake in human brain, indicating possible specific binding to SV2A in the CS. The slight specific binding to SV2A in the white matter may be due to the presence of SV2A protein in the white matter caused by the transport of synaptic vesicles or their precursors along the axon.<sup>19,20</sup> Additionally, SV2A has been reported to localize in mitochondrial membranes, albeit at a much smaller degree than in synaptic plasma membranes.<sup>21,22</sup> Though the concentration of SV2A due to these factors is likely minor, they may be contributing to all or part of the specific binding in the white matter, which is about 8% of the  $V_S$  in the gray matter. The displacement observed in the white matter could potentially be caused by the interaction of our tracer with a target other than SV2A; however, if this is the case, it is important to recognize that such sites were blocked by both antiepileptic drugs LEV and BRV, which are highly selective to SV2A.<sup>23,24</sup>

White and GM are fundamentally different tissues within the brain. GM consists of neuronal cell bodies and glial cells, while white matter is predominantly composed of myelinated axons that project from a neuronal cell body to make connections to other neurons. The myelin that surrounds the axons in white matter contributes to an overall greater lipid content of this tissue compared to GM.<sup>25</sup> Using our voxel-wise methods for  $V_{ND}$  estimation (Figure 5(d)), we found  $\sim 20\%$  higher nondisplaceable uptake in the white matter than in gray matter regions. This supports the hypothesis that, even without specific binding, the

radioligand may behave differently between the two tissue types. However, as long as these differences in tissue characteristics are consistent within and across groups, the CS region may be a valuable reference region. The subjects in this study were recruited as healthy volunteers and were evaluated using a standard screening protocol. Clinical cases of neuroinflammation, neurodegeneration, white matter lesions, or vascular burden should be studied further to evaluate the use of a white matter reference region, in particular our CS\_AAL ROI, in these populations of subjects.

Our group has shown significant differences in  $^{11}\text{C}$ -UCB-J  $V_T$  and  $BP_{ND}$ , estimated from compartment modeling and arterial input function or using SRTM2 with the CS as a reference region, in the hippocampus in AD patients compared to cognitively normal individuals.<sup>8</sup> In that study, the  $V_T$  values in the CS region were very similar between groups. Assuming that GM  $V_{ND}$  is the same in both cohorts, we can calculate the  $BP_{ND}^{\text{True}}$  using the reported  $V_T$  values and the regional  $V_{ND}$  estimates derived from the parametric images reported here. As expected, the overall  $BP_{ND}$  estimates increased from 1.54 to 3.01 in the hippocampus of cognitively normal subjects, and from 0.87 to 1.89 in the hippocampus of AD patients. However, the between-group  $BP_{ND}$  differences were similar, from 43.5% different using CS  $V_T$ , to 37.1% different using the regional hippocampus  $V_{ND}$  derived from the parametric  $V_{ND}$  maps.

Other considerations while using the CS as a reference region include the sensitivity of our measures to the partial volume effect and to inaccuracies in scatter correction. The CS ROI used in this study was small (2 mL volume) and defined to ensure no GM was included in the ROI, as well as to minimize partial volume effect by avoiding white matter voxels that lay along the gray-white matter boundary in the CS. To assess whether this CS region was subject to any partial volume effects, partial volume correction (PVC) was applied to dynamic  $^{11}\text{C}$ -UCB-J PET images using the iterative Yang's method.<sup>26</sup> This method produces a voxel-based correction by first creating a piece-wise uniform image with regional mean values, which is then convolved with the point-spread function of the system. The ratio between these images (before and after convolution) is applied to the original PET image, and the process iterates until convergence. In a subset of subjects ( $N=42$ ) used for CS ROI definition, this PVC had a minimal effect on CS values, with the baseline CS\_AAL  $V_T$  decreasing by 2.4%, from  $4.32 \pm 0.67 \text{ mL/cm}^3$  before PVC, to  $4.22 \pm 0.63 \text{ mL/cm}^3$  after PVC. Thus, we believe the optimization of our white matter ROI minimized contributions of the partial volume effect. A caveat is that the PET data in this study were acquired on a Siemens HRRT, with image

resolution of approximately 3 mm full width at half maximum. For data collected using a PET scanner that has poorer resolution, partial volume effects will likely contribute a noticeable bias in CS  $V_T$ , and thus PVC should be investigated. Note that if PVC is performed, it may be appropriate to use a larger CS ROI, to improve statistical reliability.

Scatter correction is an important aspect of PET quantification, with inaccurate scatter correction producing primarily an additive error to the images; this can produce a large percent error in low-activity regions.<sup>27</sup> For baseline  $^{11}\text{C}$ -UCB-J scans, with high gray:white contrast of  $\sim 4:1$ , scatter correction accuracy is particularly important for CS quantification. Also, inaccurate scatter correction can produce different errors in baseline and blocking scans, due to their different contrast levels. To assess the sensitivity of our results to the accuracy of the single scatter simulation (SSS) correction method, we changed the scatter parameters in the reconstruction to assess the effect on baseline CS  $V_T$  estimates. Changing the lower level discriminator in SSS from 400 keV (default) to 375 keV led to a reduction in estimated scatter fraction and an increase in a representative subject's baseline CS  $V_T$  from 4.95 to 6.11 mL/cm<sup>3</sup>. Thus, these measurements can potentially be sensitive to scatter correction and should be investigated further. As for many PET studies, scatter due to radioactivity sources that are out of the scanner field of view (FOV) may also cause inaccuracies in quantification, and corrections for this have been proposed. However, we believe that out of field (OOF) scatter will contribute minimally to image quantification for these brain images on the HRRT, as the degree of OOF scatter is a function of the amount of radioactivity and the location of the source relative to the scanner FOV.<sup>28,29</sup> In the case of  $^{11}\text{C}$ -UCB-J imaging, brain activity is very high, and based on whole body images of this tracer, there is no area in the upper body near the HRRT gantry with radioactivity levels approaching that of the brain, and thus will likely not introduce significant OOF scatter artifacts. In addition, due to the large axial FOV of the HRRT, there is typically  $\sim 5$  cm below the brain that is included in the scan. The lower axial slices in the images are incorporated in the scatter computation; OOF scatter would likely have the most effects on this region of the image, and since this is non-brain, we expect that OOF scatter will not introduce substantial bias to the brain measurements.

The midbrain region of the pons could also be considered as a potential reference region for SV2A-PET imaging with  $^{11}\text{C}$ -UCB-J. However, in previous in vitro studies including Western blot, our group reported evidence of slight concentrations of SV2A in the pons. Additionally, we find that in nine acute blocking studies

with LEV ( $N=4$ ) or BRV ( $N=5$ ), the pons has a higher average baseline  $V_T$  of 6.5 (0.4) mL/cm<sup>3</sup> and has considerable blocking upon drug administration ( $48 \pm 6\%$ ), about twice the amount in CS ( $22 \pm 6\%$ ). Additionally, on average, the baseline  $V_T$  of the pons was 164.9 ( $\pm 70.1$ )% greater than the GM  $V_{ND}$ . Thus, we believe the CS is likely to be a more valuable reference region for <sup>11</sup>C-UCB-J PET quantification.

Recent work by Koole et al.<sup>15</sup> also investigated CS as a reference region for <sup>11</sup>C-UCB-J quantification. In a study of 10 healthy subjects, baseline  $V_T$  values in the CS (denoted  $V_{SO}$ ) were reported as  $5.3 \pm 0.6$  mL/cm<sup>3</sup>, which is higher than the value reported here of  $4.58 \pm 0.74$  mL/cm<sup>3</sup>. This is expected due to the poorer resolution of the PET system used in the former study compared to the HRRT, as the resolution likely contributes to greater partial volume effects and thus a higher spill-in from high radioactivity gray matter into the white matter. At average occupancy levels of  $82.1 \pm 14.5\%$ , the average  $V_{SO}$  decreased to  $4.9 \pm 0.9$  mL/cm<sup>3</sup> during blocking scans, though this decrease of about 10% did not reach statistical significance. In our current study, we report a significant decrease between baseline and blocking  $V_T$  values in the CS, with average percent differences around 15%. When considering factors such as OS-EM convergence issues, partial volume effects, and differences in sample size and range of occupancies, our results and those of Koole et al. show considerable agreement.

Although there remains a significant difference between the CS and the  $V_{ND}$  in the gray matter of <sup>11</sup>C-UCB-J, given the correlation between these two estimates, the CS is likely a useful reference region for SV2A. Since SV2A is expressed in synaptic vesicles at virtually all synapses in the brain, there is no gray matter region available that would be devoid of the protein to allow for a true reference region to be used. Thus, the white matter, with specific uptake on the scale of less than 10% that of the gray matter, may be a valuable resource for estimating the nondisplaceable activity. Even though the CS uptake is predominantly due to nondisplaceable binding, it remains important to assess any differences in white matter uptake when investigating differences across disease groups, especially in diseases with white matter pathology.

### Funding

The author(s) disclosed receipt of the following financial support for the research, authorship, and/or publication of this article: NINDS (R01NS094253), NIA (R01AG052560), and UCB Pharma. This work was also supported by CTSA Grant Number UL1 TR000142 from the National Center for Advancing Translational Science, a component of the NIH.

### Acknowledgements

UCB Pharma provided radiolabeling precursor and the reference material for <sup>11</sup>C-UCB-J. The authors also acknowledge the staff of the Yale PET Center for their expert assistance. Its contents are solely the responsibility of the authors and do not necessarily represent the official view of NIH.


### Declaration of conflicting interests


The author(s) declared the following potential conflicts of interest with respect to the research, authorship, and/or publication of this article: SR, TT, SJF, MN, YL, NN, JR, and YH have no conflicts of interest to disclose. SDB, CO, AS, JMN, PM, JM, and RPM are employees of UCB Pharma. RC has received research support from Astellas Pharma, Astra-Zeneca, Bristol-Myers Squibb, Lilly, Pfizer, Taisho Pharmaceutical and UCB Pharma outside of the submitted work. SJF was supported by an International Postdoc grant from the Swedish Research Council.

### Authors' contributions

SR performed the experiments, data analysis and manuscript preparation, TT performed experiments and data analysis, SJF designed the study, performed the experiments, and data analysis, MN performed data analysis, YL performed data analysis, NN performed PET experiments, JR performed PET experiments, SDB designed the study, CO designed the study, AS designed the study, JMN designed the study, PM designed the study, JM designed the study, YH designed and performed the PET experiments, RPM designed the study, RC designed and performed the PET experiments, data analysis and manuscript preparation.

### ORCID iDs

Sjoerd J Finnema  <https://orcid.org/0000-0002-4972-3627>

Mika Naganawa  <https://orcid.org/0000-0002-4408-2621>

### References

- van Vliet EA, Aronica E, Redeker S, et al. Decreased expression of synaptic vesicle protein 2A, the binding site for levetiracetam, during epileptogenesis and chronic epilepsy. *Epilepsia* 2009; 50: 422–433.
- Selkoe DJ. Alzheimer's disease is a synaptic failure. *Science* 2002; 298: 789–791.
- Estrada S, Lubberink M, Thibblin A, et al. [(11)C]UCB-A, a novel PET tracer for synaptic vesicle protein 2A. *Nucl Med Biol* 2016; 43: 325–332.
- Nabulsi NB, Mercier J, Holden D, et al. Synthesis and preclinical evaluation of <sup>11</sup>C-UCB-J as a PET tracer for imaging the synaptic vesicle glycoprotein 2A in the brain. *J Nucl Med* 2016; 57: 777–784.
- Warnock GI, Aerts J, Bahri MA, et al. Evaluation of <sup>18</sup>F-UCB-H as a novel PET tracer for synaptic vesicle protein 2A in the brain. *J Nucl Med* 2014; 55: 1336–1341.
- Li S, Cai Z, Wu X, et al. Synthesis and in vivo evaluation of a novel PET radiotracer for imaging of synaptic vesicle glycoprotein 2A (SV2A) in nonhuman primates. *ACS Chem Neurosci* 2019; 10: 1544–1554.

7. Finnema SJ, Nabulsi NB, Eid T, et al. Imaging synaptic density in the living human brain. *Sci Transl Med* 2016; 8: 348ra396.
8. Chen MK, Mecca AP, Naganawa M, et al. Assessing synaptic density in Alzheimer disease with synaptic vesicle glycoprotein 2A positron emission tomographic imaging. *JAMA Neurol* 2018; 75: 1215–1224.
9. Finnema SJ, Nabulsi NB, Mercier J, et al. Kinetic evaluation and test-retest reproducibility of [(11)C]UCB-J, a novel radioligand for positron emission tomography imaging of synaptic vesicle glycoprotein 2A in humans. *J Cereb Blood Flow Metab* 2018; 38: 2041–2052.
10. Finnema SJ, Rossano S, Naganawa M, et al. A single-center, open-label positron emission tomography study to evaluate brivaracetam and levetiracetam synaptic vesicle glycoprotein 2A binding in healthy volunteers. *Epilepsia* 2019; 60: 958–967.
11. Carson RE, Channing MA, Blasberg RG, et al. Comparison of bolus and infusion methods for receptor quantitation: application to [18F]cyclofoxy and positron emission tomography. *J Cereb Blood Flow Metab* 1993; 13: 24–42.
12. Carson RE, Barker WC, Liow J, et al. Design of a motion-compensation OSEM list-mode algorithm for resolution-recovery reconstruction for the HRRT. In: *IEEE nuclear science symposium*, Portland, OR, USA, 2003, pp.3281–3285. IEEE.
13. Jin X, Chan C, Mulnix T, et al. List-mode reconstruction for the Biograph mCT with physics modeling and event-by-event motion correction. *Phys Med Biol* 2013; 58: 5567–5591.
14. Papademetris X, Jackowski MP, Schultz RT, et al. Integrated Intensity and Point-Feature Nonrigid Registration. *Med Image Comput Comput Assist Interv* 2001; 3216: 763–770.
15. Koole M, van Aalst J, Devrome M, et al. Quantifying SV2A density and drug occupancy in the human brain using [(11)C]UCB-J PET imaging and subcortical white matter as reference tissue. *Eur J Nucl Med Mol Imaging* 2019; 46: 396–406.
16. Cunningham VJ, Rabiner EA, Slifstein M, et al. Measuring drug occupancy in the absence of a reference region: the Lassen plot re-visited. *J Cereb Blood Flow Metab* 2010; 30: 46–50.
17. Hudson HM and Larkin RS. Accelerated image reconstruction using ordered subsets of projection data. *IEEE Trans Med Imaging* 1994; 13: 601–609.
18. Boellaard R, van Lingen A and Lammertsma AA. Experimental and clinical evaluation of iterative reconstruction (OSEM) in dynamic PET: quantitative characteristics and effects on kinetic modeling. *J Nucl Med* 2001; 42: 808–817.
19. Barres BA and Barde Y. Neuronal and glial cell biology. *Curr Opin Neurobiol* 2000; 10: 642–648.
20. Chevalier-Larsen E and Holzbaur EL. Axonal transport and neurodegenerative disease. *Biochim Biophys Acta* 2006; 1762: 1094–1108.
21. Stockburger C, Miano D, Baeumlisberger M, et al. A mitochondrial role of SV2a protein in aging and Alzheimer's disease: studies with levetiracetam. *J Alzheimers Dis* 2016; 50: 201–215.
22. Noyer M, Gillard M, Matagne A, et al. The novel anti-epileptic drug levetiracetam (ucb L059) appears to act via a specific binding site in CNS membranes. *Eur J Pharmacol* 1995; 286: 137–146.
23. Gillard M, Fuks B, Leclercq K, et al. Binding characteristics of brivaracetam, a selective, high affinity SV2A ligand in rat, mouse and human brain: relationship to anti-convulsant properties. *Eur J Pharmacol* 2011; 664: 36–44.
24. Lynch BA, Lambeng N, Nocka K, et al. The synaptic vesicle protein SV2A is the binding site for the anti-epileptic drug levetiracetam. *Proc Natl Acad Sci U S A* 2004; 101: 9861–9866.
25. O'Brien JS and Sampson EL. Lipid composition of the normal human brain: gray matter, white matter, and myelin. *J Lipid Res* 1965; 6: 537–544.
26. Erlandsson K, Buvat I, Pretorius PH, et al. A review of partial volume correction techniques for emission tomography and their applications in neurology, cardiology and oncology. *Phys Med Biol* 2012; 57: R119–R159.
27. Watson CC, Newport D, Casey ME, et al. Evaluation of simulation-based scatter correction for 3-D PET cardiac imaging. *IEEE Trans Nucl Sci* 1997; 44: 90–97.
28. Bentourkia M, Belakhlef A and Benard F. Determination of scatter characteristics generated from out of FOV source in FDG-PET studies. In: *1999 IEEE Nuclear Science Symposium*, Seattle, WA, 24–30 October 1999.
29. Ferreira NC, Trebossen R and Bendriem B. Assessment of the quantitation in 3D PET: Influence of out of the field of view radioactive sources. In: *1996 IEEE nuclear science symposium – conference record*, Vols. 1–3, Anaheim, CA, 2-6 November, pp.1343–1347.